Sensing and control interface for precision gap control

Michael Andonian, Robert T. M'Closkey*

Mechanical and Aerospace Engineering Department, Samueli School of Engineering and Applied Science, 420 Westwood Plaza,
University of California, Los Angeles, CA 90095

Abstract

A one degree-of-freedom precision position control system using an electrostatically actuated and capacitively sensed beam is reported. The beam is allowed to rock on a $10\,\mu$m high fulcrum which is fabricated from SU-8 deposited onto a glass substrate. The fulcrum establishes the nominal working gap between the beam and two electrodes located on the substrate. The differential capacitance formed by the beam and electrodes is sensed, however, the electrodes are also simultaneously used for applying controlled electrostatic forces to the beam. The system is unstable so feedback control is necessary to establish a desired stable gap but only after an appropriate feedforward filter that compensates for the forcer-to-pick-off coupling is implemented. The RMS displacement noise from DC to 100 Hz is 7 nm, and the gap can be regulated from DC to 600 Hz.

Keywords: electrostatic levitation, microelectromechanical system, unstable plant

---

1. Introduction

This paper describes the fabrication, analysis and testing of an unstable one degree-of-freedom (DOF) system that is aiding in the development of a platform for the electrostatic levitation of planar resonators. Electrostatically levitated microstructures have been demonstrated in the context of suspended proof masses for accelerometers and gyroscopes, eg. [1, 2, 3, 4], however, the objectives of this research are to create a tool for experimentally quantifying changes in the dynamics of planar resonators with regard to perturbations of the resonators' mass distribution and, in particular, how the motion at the stem, attachment point or anchor changes as a function of these perturbations. The notion of an "electrostatic bearing" is appealing because it represents a controllable and repeatable resonator boundary condition that does not introduce thermally-generated stresses in the resonator such as hard-mounts with thermally mismatched materials. An example of the sort of planar resonator that will be tested with such a platform is discussed in [5, 6]. This resonator was modified with post-fabrication techniques to drive two lightly damped modes to the same frequency, however, it is also desirable to quantify how the reaction at the resonator stem-substrate interface changes under such modifications. Measurements of this sort have not yet been demonstrated for microscale resonators but the electrostatic levitation platform under development can be used to quantify stem motion as a function of the perturbations made to the resonator. The levitation platform design will not be further elaborated upon other than to note that like many of the aforementioned references, the electrodes are situated in an antagonistic configuration for applying electrostatic forces to the suspended structure and

---

*Corresponding author, Tel.: 00 1 310 825 2909
Email addresses: `andonian23@g.ucla.edu` (Michael Andonian), `rtm@seas.ucla.edu` (Robert T. M'Closkey)

for detecting differential capacitances to infer structure motion. The goal of the work presented in this paper is to provide a limited degree-of-freedom structure for developing not only the forcing and pick-off interface for the levitation platform, but also a modeling and analysis framework that accurately predicts the dynamics of the 1-DOF structure so extrapolation to a multi-DOF configuration can be made with confidence and, hence, also serve as a design tool.

One feature that is common to all electrostatically levitated proof masses is the instability of the system and so a useful 1-DOF structure should preserve this property. An unstable plant is formed in the present work by considering a silicon beam that rotates on a $10\,\mu$m high fulcrum. A pair of electrodes are patterned on a glass substrate and symmetrically situated on either side of the fulcrum and below beam. They are used to apply electrostatic forces to create a net moment on the beam, but they are also designed such that zero differential capacitance indicates that the there are uniform $10\,\mu$m gaps between the beam and electrodes (Figs. 2 and A.9 show schematics of the 1-DOF system). This system has the advantage of presenting no unusual fabrication requirements, and is easy to assemble and test with different electrode configurations. Since the differential capacitance transduction and electrostatic forcing are both achieved using a single pair of electrodes, this work is closest in spirit to the scheme used by the North American Aviation Electrostatically Levitated Gyro (ESG) dating from the 1960s [7, 8]. As would be expected from an interface that uses the same electrodes as pick-offs and forcers, there is an issue of feedthrough coupling in which a control command perturbs the pick-off signal irrespective of the motion of the proof mass. The feedthrough was reduced in the ESG through the use of a model transformer, however, our approach shows how a feedforward filter implemented in the DSP achieves the same result. Another contribution of the paper is the rigorous stability analysis of the non-linear time-periodic equations of motion. In fact, the analysis of the linearized time-periodic models show remarkable agreement with the measurements made from the stabilized experimental system.

The paper is organized as follows: Sec. 2 discusses the fabrication of the beam and substrate and its interface to the balanced transformer; Sec. 3 develops a basic beam-transformer model that reveals essential features of the system dynamics but this model is further embellished to include the dynamics of all components present in the experimental system; Sec. 4 discusses the stabilizing controller design and presents the experimental results including a calibration test to determine the voltage-to-displacement scale factor from which the displacement noise spectrum is derived; Sec. 5 concludes the paper.

2. System description

2.1. Fabrication

Curvature of the beam and substrate must be minimized in order to facilitate the creation of a uniform $10\,\mu$m gap between the approximately $4\,\text{cm} \times 2.5\,\text{cm}$ beam and the substrate. These tolerances are satisfied by selecting a 1 mm thick glass substrate and a $500\,\mu$m thick silicon wafer with minimal bow and warpage. Although the surfaces are flat it is necessary to establish a nominal gap between the substrate and silicon beam. The nominal gap, denoted d_0, is specified by creating a fulcrum on which the beam will rest. The fulcrum is fabricated by first spinning a 10μm thick layer of the epoxy-based photoresist SU-8 onto the glass substrate. SU-8 is selected for its ability to create a well-defined thickness across the wafer by simply adjusting the spin coater parameters. The SU-8 is subsequently patterned, developed, and cured to create a fulcrum that is 10μm in height, $100\,\mu$m in width and 30 mm in length. With the fulcrum in place, an image reversal process is conducted to pattern the glass for the electrodes and their wire bonding pads. A $0.5\,\mu$m thick layer of gold is evaporated over a 30 nm thick Cr adhesion layer to form the electrodes on the substrate. These steps are shown in Fig. 1.

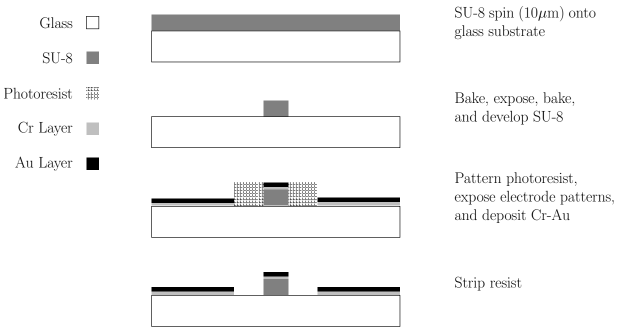

Figure 1: Processing steps for glass substrate.

The beam is diced out of a 500 μm thick, single-side polished silicon wafer. The beam is coated with a layer of aluminum ensuring excellent conductivity so the beam can be modeled as an equipotential body. Lastly, a 500 nm thick layer Parylene-C is deposited onto the beam to increase the dielectric strength of the insulating layer between the beam and the electrodes, which effectively increases the maximum possible potential difference between the electrodes and beam that may be applied before breakdown occurs. The electrodes are accessed via gold wire bond pads situated to the side of the beam. The beam also has an attached wire bond to maintain the beam at ground potential. Alignment markers on the glass simplify centering the silicon beam on the SU-8 fulcrum. The assembled system is shown in Fig. 2 where the beam is rendered semi-transparent in order to reveal the electrodes in relation to the fulcrum. The relevant dimensions are given in Table A.1. The substrate is fabricated with two pairs of electrodes, each pair possessing electrodes on opposite sides of the fulcrum. Only one pair is used in the present work as indicated in Fig. 2, however, operation of two pairs would enable maintaining the beam at ground potential without the physical ground used here.

2.2. *Electronics interface*

The beam-substrate geometry permits only small beam deflection angles so a simple parallel plate capacitor model adequately describes the relation between the capacitance and the beam-electrode gap. Specifically, this beam-electrode gap is the length of the normal vector that extends from the electrode geometric center to beam undersurface. Due to the electrode symmetry about the fulcrum, any beam deflection results in a deviation from the nominal 10μm beam-electrode gap by $\pm L\theta$, where L is the moment arm defined from electrodes' geometric center to the fulcrum and θ represents the beam angle referenced to the substrate parallel (see Fig. A.9). The transformer consists of two primary legs wound such that the two primary inductances are equal and connected together via a center tap, shown in Fig. 2 and in greater detail in Fig. A.9. The center tap is connected to a current source in which a sinusoidal current generates nominally equal charges on the electrodes which, due to the large primary inductances, are essentially independent of the electrode-beam capacitances. The beam is maintained at ground so an imbalance in the beam-electrode capacitances imposes a voltage drop, denoted v_s, across the secondary load. Thus, v_s represents a measurement of the beam orientation θ from its "balanced" configuration in which beam-electrode capacitances, and hence the gaps, are equal, i.e. the beam and substrate have parallel surfaces.

In addition to operating as a displacement transducer, the transformer simultaneously provides a means of exerting controlled electrostatic forces on the beam. By connecting resistor R_k in series with the transformer secondary, a potential v_c induces a differential potential on each electrode. In other words, the

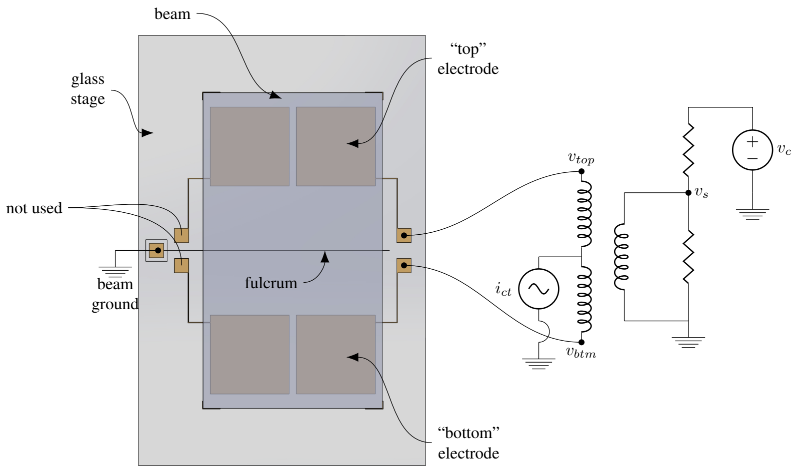

Figure 2: Schematic showing substrate, beam, fulcrum and electrodes in relation to the transformer used for differential capacitance transduction and electrostatic forcing.

electrode potentials invariably have a 180° phase difference due to the magnetic coupling between the transformer windings. As a result, if the phase of v_c is properly chosen, an imbalance in the electrostatic forces applied to the beam creates a net moment that can be exploited for control of the beam orientation. This circuit configuration, however, creates "feedthrough" from v_c to v_s, because application of v_c also develops a voltage drop across the secondary resistor. Identifying and removing this feedthrough is critical for accurately measuring the orientation of the beam and is discussed in Sec. 3.2.

3. System models and their analysis

3.1. Coupled transformer-beam subsystem

The equations of motion governing transformer voltages and currents and the equations of motion for a rigid beam constrained to rotate about the fulcrum are given in Appendix A. These equations are standard but are included for completeness. The parameters in the equations are given in Table A.1 and are used in the analysis of the models in this section. The beam and transformer equations are linked because the potentials on the electrodes create electrostatic forces on the beam, and conversely, the beam angle changes the capacitances created between the electrodes and beam. The analysis of the transformer-beam subsystem is performed in this section. The full plant model, however, also includes a DAC smoothing filter, an anti-alias filter, and a low-pass filter for recovering the baseband signal produced when the filtered v_s voltage is demodulated. Analysis of the full system is postponed until Sec. 3.2 because the proposed approach is most easily illustrated using the transformer-beam subsystem and its extension to the full system would require additional notation.

It is convenient to analyze the equations of motion using physical variables, however, for the transformer equations (A.1) this leads to an over-determined set. Nevertheless, the equations can be written as follows,

$$M(\theta)\dot{x} = Ax + B_1 i_{ct} + B_2 v_c \tag{1}$$

where the mass matrix $M(\theta) \in \mathbf{R}^{23\times23}$ is dependent on the beam angle θ and where $x \in \mathbf{R}^{23}$ is a vector whose elements are the currents and voltages shown in Fig. A.9, their ordering being unimportant for the present analysis. The matrices A, B_1 and B_2 are derived from the equations (A.1). It can be shown $\text{rank}(M) = 7$, independent of θ, so, fundamentally, there are only 7 states required for describing the evolution of the transformer currents and voltages. The beam equations are represented as

$$\frac{d}{dt}\begin{bmatrix}\theta \\ \dot{\theta}\end{bmatrix} = \begin{bmatrix}\dot{\theta} \\ f(\theta; x)\end{bmatrix} \tag{2}$$

where f is the moment applied to the beam normalized by the moment of inertia –see (A.2)

The sinusoidal center tap current, $i_{ct}(t) = a_{ct}\cos(\omega_0 t)$, is produced by a current source, where a_{ct} is the amplitude and ω_0 is the carrier frequency. When the beam orientation is $\theta = 0$, the capacitances created between the electrodes and beam are equal in the beam model, i.e. $C_{top} = C_{btm}$. In this case i_{ct} establishes steady-state sinusoids for all signals in the transformer as well as a master phase angle against which all steady-state signals are referenced. The steady-state response of the currents and voltages in the transformer, denoted x_0, are computed from the frequency response of (1) with $v_c = 0$

$$x_0(t) \overset{r}{=} (j\omega_0 M(0) - A)^{-1} B_1 a_{ct} e^{j\omega_0 t}. \tag{3}$$

Despite the fact that $M(0)$ is not invertible, the matrix $j\omega_0 M(0) - A$ is invertible for any $\omega_0 \neq 0$. For this steady-state solution the electrode potentials are equal sinusoids, i.e. $v_{top}(t) = v_{btm}(t)$, and so $f(0; x_0(t)) = 0$ for all t. Thus, x_0 along with $\theta(t) = 0$ and $\dot{\theta}(t) = 0$ represent a periodic solution for the coupled transformer-beam subsystem. The beam is in equilibrium because the net beam moment produced by the electrostatic forces is zero and the beam center of mass is assumed to be located at the fulcrum. The stability of this periodic solution can be studied by analyzing the linear variational equations of (1) and (2) –refer to [9] for terminology.

The variational equations can be determined by introducing perturbation variables relative to their steady-state values: $x = x_0 + \delta_x$, $\theta = 0 + \delta_\theta$ and $\dot{\theta} = 0 + \delta_{\dot{\theta}}$. The effect of the control voltage v_c can also be included in the analysis by setting $v_c = 0 + \cos(\omega_0 t + \phi_{v_c})\delta_{v_c}$. Since i_{ct} and v_c have the same carrier frequency, v_{top} and v_{btm} are sinusoidal with frequency ω_0, however, the i_{ct}-induced components create in-phase potentials on v_{top} and v_{btm}, while the v_c-induced components have a 180° phase relationship with each other. The phase of the control signal ϕ_{v_c}, however, is selected so that the v_c-induced component of v_{top} is in-phase with the i_{ct}-induced sinusoid and, thus, the v_c-induced component of v_{btm} is 180° out of phase with the i_{ct}-induced component. Thus, when the center tap current is driving the transformer, changing the v_c amplitude, i.e. δ_{v_c}, will create a *differential* change in the *amplitudes* of v_{top} and v_{btm}, and because the electrostatic forces are proportional to the mean-square electrode voltages, this differential change in the amplitudes creates the largest moment on the beam for a given value of δ_{v_c}.

The mass matrix is continuously differentiable in a neighborhood of $\theta = 0$ and so is represented as $M(\theta) = M(0) + M_\theta \delta_\theta + \cdots$, where $M_\theta := \frac{\partial M}{\partial \theta}|_{\theta=0}$. Substituting these expressions into (1) and (2) and retaining only linear terms yields the following variational equations,

$$\begin{aligned} M(0)\dot{\delta}_x &= A\delta_x - M_\theta \dot{x}_0 \delta_\theta + B_2 \cos(\omega_0 t + \phi_{v_c})\delta_{v_c} \\ \frac{d}{dt}\begin{bmatrix}\delta_\theta \\ \delta_{\dot{\theta}}\end{bmatrix} &= \begin{bmatrix}\delta_{\dot{\theta}} \\ f_\theta \delta_\theta + f_x \delta_x\end{bmatrix}, \end{aligned} \tag{4}$$

where $f_\theta := \frac{\partial f}{\partial \theta}(0; x_0)$ and $f_x := \nabla_x f(0; x_0)$ are the gradients of f with respect to θ and x evaluated on the periodic solution. These equations are time periodic with period $\tau_p = 2\pi/\omega_0$. The algebraic constraints in (4) must be resolved and this is accomplished with a coordinate change. Let a singular value decomposition of $M(0)$ be

$$M(0) = \underbrace{\begin{bmatrix} U_1 \; U_2 \end{bmatrix}}_{U} \begin{bmatrix} \Sigma_1 & 0 \\ 0 & 0 \end{bmatrix} \underbrace{\begin{bmatrix} V_1^T \\ V_2^T \end{bmatrix}}_{V^T}$$

where U and V are unitary, $U_1 \in \mathbf{R}^{23\times 7}$, $V_1 \in \mathbf{R}^{23\times 7}$, $\Sigma_1 \in \mathbf{R}^{7\times 7}$ is positive definite, and so forth. New perturbation variables are defined according to

$$\delta_x = \begin{bmatrix} V_1 & V_2 \end{bmatrix} \begin{bmatrix} \delta_1 \\ \delta_2 \end{bmatrix}$$

where the dimensions of δ_1 and δ_2 are compatible with the partitioning of V. Substituting this relation into the first expression in (4) yields the differential equation and a set of explicit algebraic constraints,

$$\begin{aligned} \Sigma_1 \dot{\delta}_1 &= U_1^T A V_1 \delta_1 + U_1^T A V_2 \delta_2 - U_1^T M_\theta \dot{x}_0 \delta_\theta + U_1^T B_2 \cos(\omega_0 t + \phi_{v_c}) \delta_{v_c} \\ 0 &= U_2^T A V_1 \delta_1 + U_2^T A V_2 \delta_2 - U_2^T M_\theta \dot{x}_0 \delta_\theta + U_2^T B_2 \cos(\omega_0 t + \phi_{v_c}) \delta_{v_c} \end{aligned},$$

where $U_2^T A V_2$ is invertible so δ_2 can be expressed in terms of δ_1, δ_θ and δ_{v_c}. The matrix $P \in \mathbf{R}^{23\times 23}$ is defined to be $V_2 \left(U_2^T A V_2 \right)^{-1} U_2^T$. Thus, the linear time-periodic differential equations are derived,

$$\begin{aligned} \dot{\delta}_1 &= \Sigma_1^{-1} U_1^T \left(I - AP \right) \left(A V_1 \delta_1 - M_\theta \dot{x}_0 \delta_\theta + B_2 \cos(\omega_0 + \phi_{v_c}) \delta_{v_c} \right), \\ \dot{\delta}_\theta &= \delta_{\dot{\theta}}, \\ \dot{\delta}_{\dot{\theta}} &= \left(f_\theta + f_x P M_\theta \dot{x}_0 \right) \delta_\theta + f_x \left(I - PA \right) V_1 \delta_1 - f_x P B_2 \cos(\omega_0 t + \phi_{v_c}) \delta_{v_c}. \end{aligned} \tag{5}$$

Collecting the variables δ_1, δ_θ and $\delta_{\dot{\theta}}$ into a single 9-element state vector denoted δ, produces the following compact representation of the linear variational equations,

$$\dot{\delta} = \tilde{A}(t)\delta + \tilde{B}(t)\delta_{v_c}, \tag{6}$$

where $\tilde{A}$ and $\tilde{B}$ can be determined from (5) and both are time-periodic with period τ_p. The state transition matrix $\Phi(t, t_0)$ for this periodic system must be numerically computed. The characteristic multipliers associated with (5), which are the eigenvalues of $\Phi(\tau_p, 0)$, determine the stability of the periodic solution derived earlier. Although the experimental results are reported in Sec. 4, the analysis in this section uses transformer parameter values obtained from tests performed with an impedance analyzer. The beam parameters, on the other hand, are simply estimated from the material properties and dimensions of the beam, electrodes and fulcrum. All parameters are reported in Table. A.1. Using these parameters, the characteristic multipliers are shown in Fig. 3 for the case $\omega_0 = 25\,\mathrm{kHz}$ and $a_{ct} = 4\,\mathrm{mA}$. The period is $\tau_p = 1/\omega_0$. There is one unstable eigenvalue and one eigenvalue equal to 1. There are also four eigenvalues clustered near the origin. The eigenvalue at 1 corresponds to an integrator in the transformer. In fact, A in (1) has one eigenvalue equal to 0 which produces the characteristic multiplier equal to 1 in this analysis. The integrator corresponds to a non-zero charge which can exist in the system even when $i_{ct} = 0$ and $v_c = 0$. The charge creates constant potentials $v_{top} = v_{btm} = v_1 = v_2 = v_{ct}$, with all other potentials and currents being zero. This mode can be ignored, however, because the current source suppling i_{ct} controls this charge and, furthermore, any parasitic resistance between the center tap and ground, which exists in practice, will drain off any DC charge and thereby perturb this characteristic multiplier to lie slightly inside the unit circle. When deriving a transfer function model, it will be shown that the integrator is practically uncontrollable from v_c and hence a zero will be located at 1. Of greater interest are the pair of real characteristic multipliers located

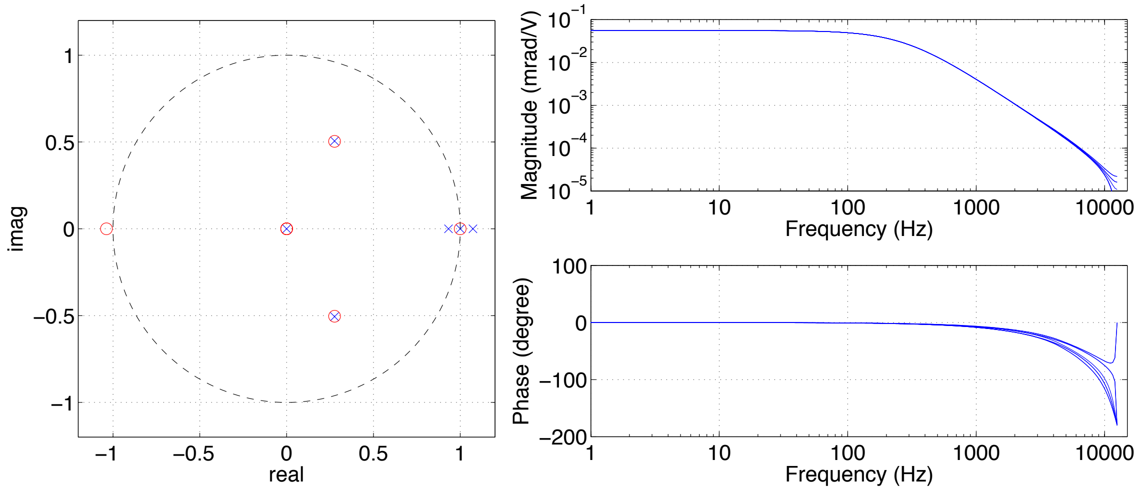

Figure 3: (Left) Characteristic multipliers of transformer-beam subsystem (×) and zeros of the approximate transfer function (○) associated with the measurement of θ for $t_0 = 0$. (Right) Approximate transfer functions with beam angle θ output for $t_0/\tau_p = 0, 0.1, 0.2, \ldots, 0.8, 0.9$.

near 1. Their continuous-time representation corresponds to real poles located at approximately $\pm 280\,\text{Hz}$. The beam dynamics in the absence of the electrode potentials is a double integrator so "connecting" the beam to the transformer with the specified center tap current bifurcates the poles to $\pm 280\,\text{Hz}$. Thus, wide bandwidth control is required to stabilize the system.

The loop shaping controller design in Sec. 4.2 requires frequency response plots from the control input to the pick-off signal. The full system dynamics are addressed in Sec. 3.2 but the approach for deriving an approximate frequency response function is first demonstrated using (6), however, since (6) is time-varying, a frequency response function does not exist for this system in a strict sense. Nevertheless, the beam dynamics evolve on a slower time scale than the transformer states as suggested by the poles at $\pm 280\,\text{Hz}$ compared to the carrier frequency of $\omega_0 = 25\,\text{kHz}$ for the transformer currents and potentials. The solution to an initial value problem for (6) is

$$\delta(t) = \Phi(t, t_0)\delta(t_0) + \int_{t_0}^{t} \Phi(t,\tau)\tilde{B}(\tau)\delta_{v_c}(\tau)d\tau, \quad t \geq t_0,$$

where $\delta(t_0)$ is the initial condition represented in the perturbation variables and δ_{v_c} is the control voltage input. An approximate time-invariant system can be derived by assuming the control variable is slowly varying over one period of the carrier frequency. Under this assumption, δ_{v_c} is pulled out of the integral so the state can be estimated one period later,

$$\delta(\tau_p + t_0) \approx \Phi(\tau_p + t_0, t_0)\delta(t_0) + \left(\int_{t_0}^{\tau_p + t_0} \Phi(\tau_p + t_0, \tau)\tilde{B}(\tau)d\tau\right)\delta_{v_c}(t_0).$$

Thus, the evolution of the states can be approximated by a discrete time equation $\delta[k+1] = \Gamma\delta[k] + \Psi\delta_{v_c}[k]$, where

$$\Gamma := \Phi(\tau_p + t_0, t_0), \quad \Psi := \int_{t_0}^{\tau_p + t_0} \Phi(\tau_p + t_0, \tau)\tilde{B}(\tau)d\tau$$

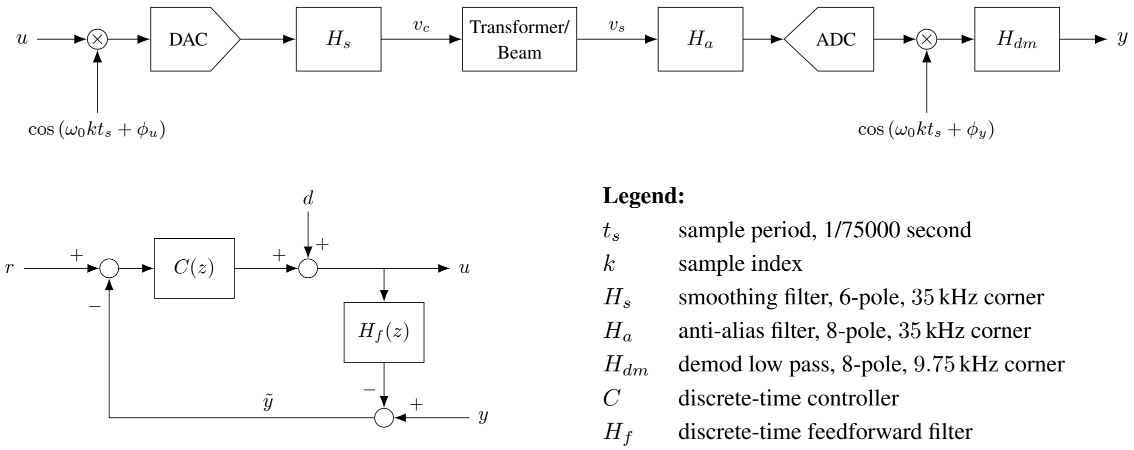

Legend:

t_s	sample period, 1/75000 second
k	sample index
H_s	smoothing filter, 6-pole, 35 kHz corner
H_a	anti-alias filter, 8-pole, 35 kHz corner
H_{dm}	demod low pass, 8-pole, 9.75 kHz corner
C	discrete-time controller
H_f	discrete-time feedforward filter

Figure 4: Block diagram of plant, controller and feedforward filter.

The notation $\delta[k]$ refers to the value of the state δ at the kth sample instant. Note that the sample instants are defined as integer multiples of τ_p relative to t_0. Thus, the approximate models are developed for different phases of the "master" reference signal $\cos(\omega_0 t)$. Although Γ and Ψ depend on t_0 (which may be restricted to the interval $[0, \tau_p)$ without loss of generality) the eigenvalues of Γ are independent of t_0, thus, the poles of the discrete-time system are the characteristic multipliers of the linear variational equations. The zeros, on the other hand, are dependent on the choice of t_0, however, their effect is most easily understood by comparing the frequency responses of the discrete-time systems obtained at different values of t_0 –this comparison is made in Figure 3 for a handful of t_0 when the output variable is selected as θ. The Nyquist frequency associated with these discrete-time models is 12.5 kHz so the frequency responses are computed up to this limit. The family of frequency responses demonstrates that the t_0 parameter only has an effect on the high-frequency aspects of the discrete-time models and for this reason the nominal model when $t_0 = 0$ will be used for the controller design. The pole-zero plot in Fig. 3 also shows that the mode with characteristic multiplier equal to 1 is cancelled by a zero. Further analysis of Γ and Ψ confirms that this mode is uncontrollable from δ_{v_c}.

3.2. Full plant model

The key aspects of the system have been analyzed in Sec. 3.1, however, the beam angle θ is not directly measured but instead inferred from measurements of v_s. Indeed, the transformer is configured as a differential capacitance transducer in which a change in the beam angle induces a differential change in the nominal electrode capacitances which in turn produces an amplitude modulated sinusoid with frequency ω_0 at v_s. Thus, a component missing from the analysis in Sec. 3.1 is the demodulation process for recovering the amplitude of v_s. Furthermore, the DSP controller implementation requires the insertion of a DAC analog smoothing filter and an anti-alias filter –the block diagram of the full plant model is shown in Fig. 4. The analysis method introduced in Sec. 3.1 can be applied here, too, because there also exists a periodic solution with $\theta(t) = 0$ and $\dot{\theta}(t) = 0$ about which linear variational equations can be developed. The DAC conversion process can be ignored in the analysis because the assumption of slow variation in u essentially introduces zero-order-hold dynamics into the discrete-time equations derived from the linear variational equations. Similarly, the band-limiting nature of the anti-alias filter ensures the spectrum of its

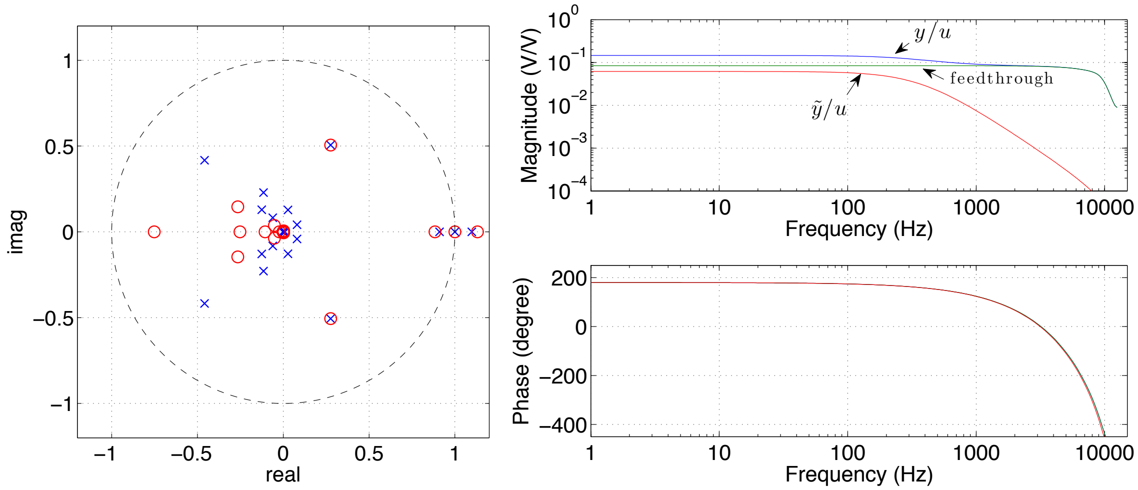

Figure 5: (Left) Poles, displayed as ×, and zeros, displayed as ○, for the 31-state discrete-time plant in Fig. 4. The zeros are computed for $t_0 = 0$. (Right) Frequency responses of discrete-time models y/u, $\tilde{y}/u$ and the feedthrough when $t_0 = 0$. The "sample rate" for the models is the frequency ω_0.

analog output is equal to that of the sampled signal produced by the ADC. Computing the models, though, requires specification of the modulation/demodulation phases ϕ_u and ϕ_y shown in Fig. 4. As described in Sec. 3.1, ϕ_u is specified so that u produces amplitude modulated sinusoids at the electrodes that possess $0°$ or $180°$ phases with respect to the sinusoids produced by i_{ct}. Similarly, the demodulation phase ϕ_y is chosen so that the amplitude modulated voltage created at v_s due to $\theta \neq 0$ is in-phase with $\cos(\omega_0 t + \phi_y)$. This choice maximizes y for a given angle θ.

The full plant model is a 31-state system: 9 states are contributed by the coupled transformer-beam subsystem, 8 states are each contributed by the analog anti-alias filter and discrete-time demodulator's low-pass filter, and 6 states are present in the DAC smoothing filter. The details of adding these components and analyzing the subsequent linear variational equations are left to the reader, however, the characteristic multipliers, estimated zeros (for $t_0 = 0$), and transfer functions y/u are shown in Fig. 5 for the case $i_{ct} = a_{ct}\cos(\omega_0 t)$, where $a_{ct} = 4\,\text{mA}$ and $\omega_0 = 25\,\text{kHz}$. One notable feature in the frequency response is the presence of a flat pass-band above $1\,\text{kHz}$ due to the coupling of v_c to v_s. This feedthrough coupling obscures the beam response at higher frequencies and biases the measurement of the beam deflection at low frequencies. It is also the source of the zeros near 1 in Fig. 5. Note that the unstable near pole-zero cancellation has implications for the achievable minimum peak sensitivity function [10]. Fortunately, the feedthrough can be identified and mitigated with an appropriate feedforward filter as described in Sec. 4. For the model, however, the feedthrough can be determined from the full plant by constraining $\theta(t) = 0$ which removes the beam dynamics from the analysis. The feedthrough frequency response is also shown in Fig. 5 along with the frequency response $\tilde{y}/u$ which reveals the anticipated -40db/decade roll-off, cf. Fig. 3. The additional filtering, however, also adds significant phase lag in the region where the loop gain is likely to cross over. The model also yields a scale factor that converts y into an equivalent gap change at the center of the electrodes (assuming parallel plate models for C_{top} and C_{btm}). The scale factor is estimated to be $10.9\,\mu\text{m/V}$. The corresponding scale factor for converting y into the beam angle is $0.706\,\text{mrad/V}$.

4. Experimental results and discussion

4.1. Test environment

The beam and glass substrate are placed in a vacuum chamber which typically pumps down to less than $10\,\mu$Torr because when the beam is operated in air, the squeeze film damping between it and the substrate vastly attenuates the response of the beam above 1 Hz. Thus, high-bandwidth control of the beam angle and beam-electrode gap is only possible *in vacuo*. In fact, the beam equations ignore all damping and are only appropriate for describing the beam in a vacuum. In any case, a levitated resonator would be operated in a high vacuum, too. The transformer, on the other hand, is located outside of the vacuum chamber and is interfaced to a DSP operating at a 75 kHz sample rate. The DSP generates the $\omega_0 = 25\,$kHz reference sinusoid for the center tap current i_{ct} and modulated signal that specifies v_c. It is clear why the smoothing filter is required since there are only three samples in one period of the carrier sinusoids. Furthermore, the Nyquist frequency is only 12.5 kHz away from ω_0 so this determines the corner frequency of the anti-alias filter in Fig. 4.

4.2. Stabilized system

Based on the θ-output transfer function in Fig. 3, constant gain feedback of sufficient magnitude will stabilize the system, but because v_s, not θ, is used for feedback, the feedthrough coupling is an impediment to stabilization due to its high gain at frequencies well beyond those at which the beam responds. Thus, the severity of the feedthrough must be reduced. This was accomplished in [7, 8] through the use of a “model transformer”, which is an analog implementation of a feedforward cancellation filter. The model transformer, as the name suggests, requires additional hardware so the alternative approach used in this work employs a discrete-time feedforward cancellation filter, denoted H_f, that is implemented in the DSP as shown in Fig. 4. Although models of the feedthrough dynamics are available, the feedthrough is experimentally identified in practice because it produces much better matching. The beam is not perfectly balanced so in the absence of stabilizing feedback control it tilts to one side with one end resting on the glass substrate. With no applied center tap current, u produces a small disturbance torque that will not move the beam from its rest position. Thus, the resulting y signal is almost entirely produced by the feedthrough coupling. This permits the identification of an appropriate model of the feedthrough. A 7-state discrete-time model of the feedthrough is implemented as H_f in Fig. 4 and is effective in reducing the feedthrough by about an order of magnitude. The beam is modeled as a rigid structure, however, there are flexural modes that can be excited and measured by the electrical interface, but since these modes tend to be somewhat symmetric about the fulcrum in mode shape, the differential sensing and forcing tends to weakly excite/sense these modes. Nevertheless, the presence of flexural modes creates a potential source of instability for any controller design since the flexural mode damping is extremely low in the vacuum.

The primary control design objective is stabilization of the unstable plant, and the analytical models developed in Sec. 3.2 are useful for guiding the initial design process. Classical loop shaping controller design is effective since the system is single-input/single-output. The plant has one unstable pole so the loop gain must have one net counter-clockwise encirclement of $-1 + j0$ in the Nyquist plot. This is achieved with a mild phase-lead filter, however, a notch is also required to reduce the magnitude of a flexural mode that exists when the beam is balanced on the fulcrum. Once the experimental system is stabilized it is possible to identify improved models by testing the closed-loop system. The empirical open-loop plant frequency response is shown in Fig. 6. Both the y/u and $\tilde{y}/u$ frequency responses have excellent agreement with the analytical model frequency responses in Fig. 5. The feedthrough filter H_f cannot be expected to provide the degree of feedthrough cancellation at high frequencies as in the case of the analytical model and, indeed, an order of magnitude reduction in the feedthrough appears to be practical as shown in Fig. 6 (compare the

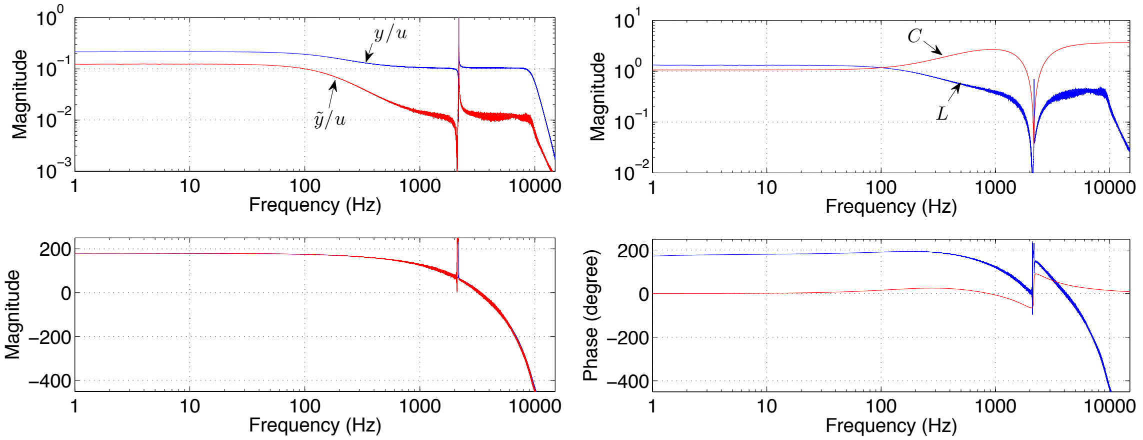

Figure 6: (Left) Open-loop empirical plant frequency responses extracted from closed-loop data. (Right) Empirical loop gain L and analytical controller frequency response (the controller magnitude is $10\times$ that shown).

relative magnitudes at high frequencies). The closed-loop frequency responses are deduced from testing the asymptotically stable closed-loop system by injecting a broadband signal where d enters the loop and then computing the cross-spectra between d all signals of interest. Open-loop frequency responses are then algebraically computed from the closed-loop frequency responses.

The presence of the residual feedthrough limits the amount of phase lead that can be added to the loop by the controller because the low frequency gain of the loop must be large enough to achieve the requisite encirclement for closed-loop stability. Also note that a notch filter is required to reduce the gain of the flexural mode near 2 kHz. An integrator is also present in the controller but its closed-loop time constant is approximately 1 second. The frequency response of the controller is shown in Fig. 6 along with the empirically measured loop gain. The cross-over frequency is approximately 150 Hz. The Nyquist plot of the experimentally measured loop gain is shown in Fig. 7 and gives more insight into the achievable stability margin. Given the limits on the high-frequency gain in the controller, the phase lead cannot reduce the sensitivity function magnitude over a large frequency band. In fact, the residual feedthrough coupled with the significant phase lag introduced by the analog filtering, creates a scenario in which large sensitivity magnitude is unavoidable over a significant frequency interval as shown in Fig. 7. Nevertheless, based on the complementary sensitivity T, the beam can track reference commands up to 600 Hz. The disturbance rejection properties of the controller, however, do suffer from the relatively large sensitivity. This raises some interesting system design questions that will be addressed in future papers.

Careful contrast of the empirical frequency responses in Fig. 6 to the analytical model frequency responses in Fig. 5 show differences in the overall magnitudes by roughly a factor of two. This difference can be attributed to how the lumped circuit parameters of the analytical model are measured and modeled. Specifically, the numerical value of the parasitic winding-to-winding capacitance, C_{w_1} and C_{w_2}, substantially effect the model frequency response magnitude and adjusting these values can show improved agreement between the two frequency responses.

4.3. Pick-off calibration and displacement noise spectrum

The voltage measurement of the beam displacement is calibrated with a laser vibrometer by placing the vibrometer spot at the center of an electrode. The vibrometer measures the velocity normal to the beam so the

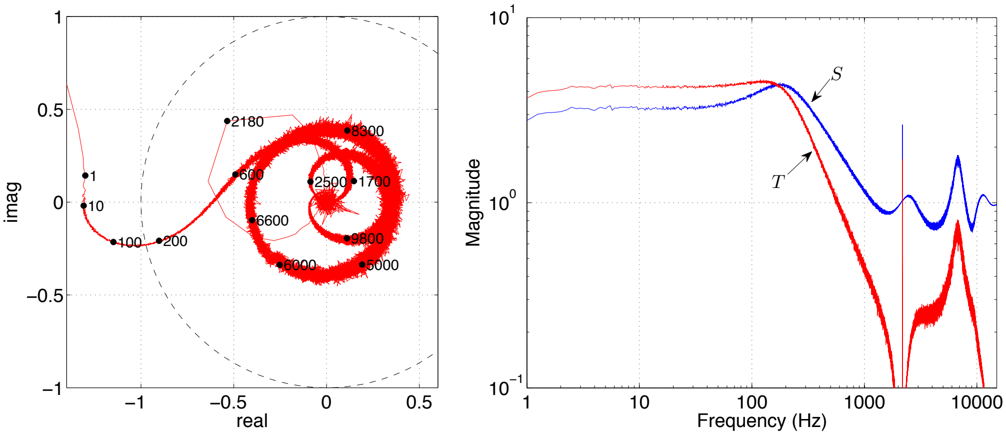

Figure 7: (Left) Nyquist plot of loop gain. (Right) Sensitivity function and complementary sensitivity function magnitudes.

closed-loop frequency response from d to the vibrometer output provides a direct measurement of the time-rate-of-change of the beam-electrode gap at the electrode center. This frequency response is “integrated” into an equivalent displacement as a function of the voltage d as shown in Fig. 8. This is compared to the closed-loop frequency response from d to the electrical pick-off measurement of the beam displacement, i.e. $\tilde{y}/d$. As the input associated with both frequency responses is the same, the low-frequency ratio of the frequency response magnitudes provides the “scale factor” associated with the electrical pick-off. This scale factor is approximately $11.5\,\mu\mathrm{m}/\mathrm{V}$ and is nearly equal to the value derived from the model and reported in Sec. 3.2. This conversion factor is accurate from DC to approximately 200 Hz, but beyond 200 Hz, the vibrometer frequency response must be normalized by the electrical pick-off frequency response, $\tilde{y}/d$. Despite the deviation from a simple gain conversion at higher frequencies, the voltage noise spectrum of $\tilde{y}$ can be scaled into an equivalent displacement noise spectrum that will be accurate for frequencies below 200 Hz. The voltage noise spectrum of $\tilde{y}$ is measured when $d = 0$, however, as the feedback loop is closed, any electrical noise will be shaped by the sensitivity function. Furthermore, any mechanical disturbances to the beam, i.e. vibration transmitted through the vacuum chamber to the beam by pumps, floor motion, etc., will also be included in the noise spectrum. The measured spectral density is shown in Fig. 8 and reveals that the RMS displacement noise from DC to 100 Hz is approximately 7 nm. The largest contributions appear to be from line noise near 50-60 Hz, and subharmonics. Discounting these components reveals a noise floor near $0.1\,\mathrm{nm}/\sqrt{\mathrm{Hz}}$. Thus, the beam motion can be measured with a high precision over broad frequency band.

There are other interesting features in the vibrometer data. For example, the lightly damped flexural mode near 2 kHz is evident in the frequency and the noise spectrum, thus, as noted above, the displacement noise spectrum also includes acceleration disturbances to the beam in addition to electrical noise. The vibrometer also appears to detect additional flexural modes near 1.3 kHz and 9 kHz which are not detected by the electrical pick-off. This is of interest because the pick-off and forcing is collocated at the same electrode and so it should be possible to excite a flexural mode if only it can be sensed; the nature of these flexural modes and why they are excited but not sensed has not been resolved.

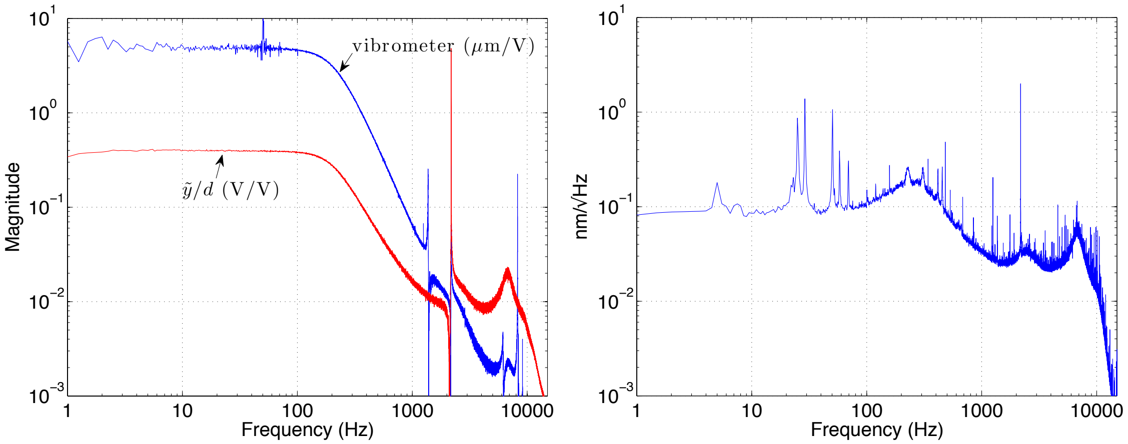

Figure 8: (Left) Vibrometer measurements for calibrating electrical pick-off. (Right) Displacement noise spectrum of $\tilde{y}$ using scale factor obtained from the vibrometer data.

5. Conclusion

Modeling, analysis, and test results are reported for a precision gap control system using an electrostatically actuated and capacitively sensed beam and represents a step towards the creation of a testbed for fully levitated resonators. The model analysis technique generates state-space models of the plant whose frequency responses show excellent agreement with the experimentally measured plant properties. The experiments also reveal the practical limit of compensating the feedthrough with an fixed digital filter. Finally, calibration of the beam motion with a vibrometer yields useful information on the displacement noise power spectrum. These data are important for extending the 1-DOF model to the multi-DOF configuration that is necessary for fully levitated structures.

The 1-DOF beam coupled to the transform is an unstable system when the transformer is driven by a sinusoidal center tap current and so the essential feature of the stabilizing controller is its phase-lead behavior along with its sufficiently large low frequency gain. The residual feedthrough that remains after the feedforward cancellation, however, limits the amount of phase lead that can be developed which, coupled with the significant plant phase lag, creates a situation in which the sensitivity function magnitude is close to 4 over a broad frequency band. Thus, although the closed-loop system is stable, it generally has poor disturbance rejection properties. Future directions will investigate methods to reduce the plant phase lag including analog modulation/demodulation in which the DSP is only used for baseband control. Furthermore, it may be possible to improve the level of feedthrough cancellation using an adaptive feedforward filter because injecting a sinusoidal signal at u that is in quadrature with $\cos(\omega_0 t + \phi_u)$ will essentially perturb the phases of v_{top} and v_{btm} but leave their amplitudes largely intact. Thus, this technique will minimally perturb the electrostatic forces on the beam but create a coupling signal to y which can be used to quantify the feedthrough. These results will be reported in future publications.

Acknowledgement: The authors thank the staff of the UCLA Nanoelectronics Research Facility. This research did not receive any specific grant from funding agencies in the public, commercial, or not-for-profit sectors.

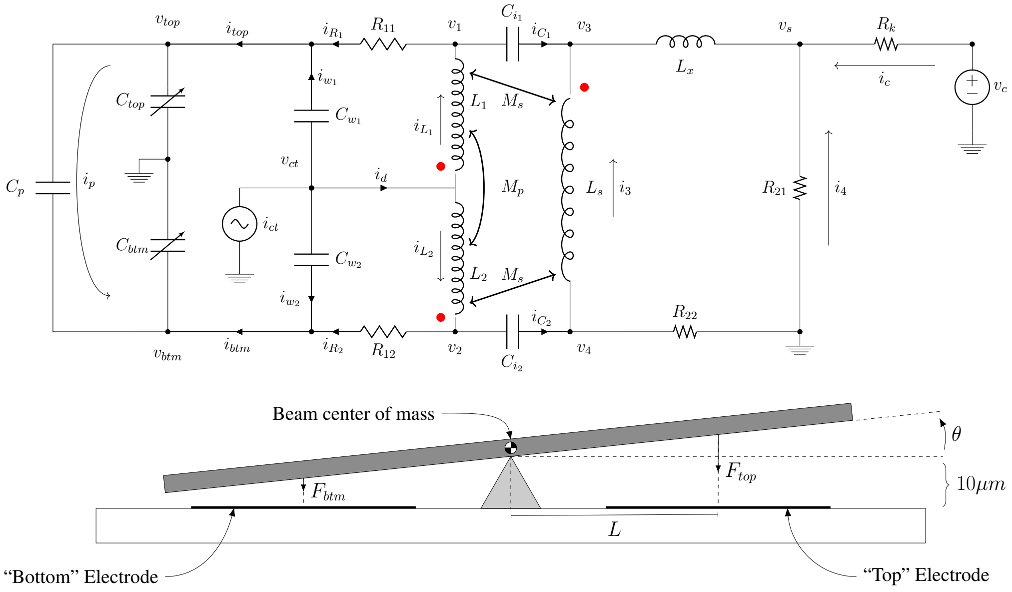

Figure A.9: (Top) Circuit representing the transformer used for sensing the beam angle and for applying electrostatic forces to the beam. (Bottom) Side view of beam in relation to electrodes (not to scale).

Appendix A. Equations of motion

The equations relating the currents and potentials in the transformer shown in Fig. A.9 are

$$\begin{aligned}
L_1\dot{i}_{L_1} - M_p\dot{i}_{L_2} - M_s\dot{i}_3 &= v_{ct} - v_1 & i_d &= i_{L_1} + i_{L_2} & C_{w_2}\left(\dot{v}_{ct} - \dot{v}_{btm}\right) &= i_{w_2} \\
L_2\dot{i}_{L_2} - M_p\dot{i}_{L_1} + M_s\dot{i}_3 &= v_{ct} - v_2 & i_{top} &= i_{w_1} + i_{R_1} & C_{i_1}\left(\dot{v}_1 - \dot{v}_3\right) &= i_{C_1} \\
L_s\dot{i}_3 - M_s\dot{i}_{L_1} + M_s\dot{i}_{L_2} &= v_4 - v_3 & i_{btm} &= i_{w_2} + i_{R_2} & C_{i_2}\left(\dot{v}_2 - \dot{v}_4\right) &= i_{C_2} \\
L_x(\dot{i}_3 + \dot{i}_{C_1}) &= v_3 - v_s & i_c &= -(i_3 + i_{C_1}) - i_4 & i_{w_1} + i_{w_2} + i_d &= i_{ct} \\
C_{top}\dot{v}_{top} &= i_{top} - i_p & i_{L_1} &= i_{R_1} + i_{C_1} & R_{22}(i_{C_2} - i_3) &= v_4 \\
C_{btm}\dot{v}_{btm} &= i_{btm} + i_p & i_{L_2} &= i_{R_2} + i_{C_2} & C_p\left(\dot{v}_{top} - \dot{v}_{btm}\right) &= i_p \\
v_1 - v_{top} &= R_{11}i_{R_1} & -R_{21}i_4 &= v_s & C_{w_1}\left(\dot{v}_{ct} - \dot{v}_{top}\right) &= i_{w_1} \\
v_c - v_s &= R_k i_c & v_2 - v_{btm} &= R_{12}i_{R_2},
\end{aligned} \tag{A.1}$$

where the inductances, resistances and capacitances are given in Table A.1. The currents and potentials in (A.1) are gathered into the vector x. The beam equations of motion are

$$\frac{d}{dt}\begin{bmatrix}\theta \\ \dot{\theta}\end{bmatrix} = \begin{bmatrix}\dot{\theta} \\ f(\theta; x)\end{bmatrix}, \tag{A.2}$$

Transformer Parameters

Parameter	Value	Parameter	Value	Parameter	Value
L_1	2.1 H	C_{top}	variable	C_{i_2}	40 pF
L_2	2.1 H	C_{btm}	variable	R_{11}	504 Ω
L_s	1.53 mH	C_p	17 pF	R_{12}	504 Ω
L_x	2.47 μH	C_{w_1}	80 pF	R_{22}	0.54 Ω
M_p	2.1 H	C_{w_2}	80 pF	R_{21}	100 Ω
M_s	57.6 mH	C_{i_1}	40 pF	R_k	100 Ω

Beam Parameters

Parameter	Value
beam length	44 mm
beam width	25 mm
beam thickness	500 μm
electrode area, A	1.21 cm^2
dielectric constant, ϵ	8.85×10^{-12} F $\cdot$ m^{-1}
fulcrum/electrode distance, L	1.55 cm
nominal beam/electrode gap, d_0	10 μm
moment of inertia, J	0.207×10^{-6} kg $\cdot$ m^2

Table A.1: Table of system parameter values

where θ represents the angle that the beam makes with respect to plane of the glass substrate on which the electrodes are deposited, i.e. the beam is parallel to the baseplate when $\theta = 0°$, and where

$$f(\theta; x) = \frac{L}{J}\left(\underbrace{-\frac{\epsilon A}{2}\frac{v_{top}^2}{(d_0 + L\theta)^2}}_{F_{top}} + \underbrace{\frac{\epsilon A}{2}\frac{v_{btm}^2}{(d_0 - L\theta)^2}}_{F_{btm}} \right).$$

Note that v_{top} and v_{btm} are elements of the vector x, and F_{top} and F_{btm} represent the electrostatic forces exerted on the beam from their respective electrodes (see Fig. A.9). The beam is grounded and the electrostatic forces produced by each electrode create a moment on the beam. The beam moment of inertia is given by J and the area of each electrode is A. The values of the beam parameters are also given in Table A.1. The transformer capacitances, denoted C_{top} and C_{btm}, depend on the beam angle and provides the link from the beam dynamics to the the transformer dynamics,

$$C_{top} = \frac{\epsilon A}{d_0 + L\theta}, \quad C_{btm} = \frac{\epsilon A}{d_0 - L\theta} \tag{A.3}$$

The parallel plate capacitance formula is used for computing these capacitances (and computing the electrostatic forces in (A.2)) even when beam is deflected. The gap for the deflected beam is computed as the product of the distance L from the fulcrum to the electrode centroid with the beam angle θ which is then summed with, or subtracted from, the nominal gap d_0. Since θ is very small even at full deflection it is not necessary to use trigonometric functions to express the gap.

References

[1] V. Josselin, P. Touboul, and R. Kielbasa, “Capacitive detection scheme for space accelerometers applications,” *Sensors and Actuators A: Physical*, vol. 78, no. 23, pp. 92 – 98, 1999.

[2] F. T. Han, Z. Gao, and Y. Wang, “A differential capacitance to voltage converter for electrostatic levitation applications,” *Sensors and Actuators A: Physical*, vol. 99, no. 3, pp. 249 – 255, 2002.

[3] R. Toda, N. Takeda, T. Murakoshi, S. Nakamura, and M. Esashi, “Electrostatically levitated spherical 3-axis accelerometer,” in *Technical Digest. MEMS 2002 IEEE International Conference. Fifteenth IEEE International Conference on Micro Electro Mechanical Systems (Cat. No.02CH37266)*, Jan 2002, pp. 710–713.

[4] M. V. Gindila and M. Kraft, “Electronic interface design for an electrically floating micro-disc,” *J. Micromech. Microeng.*, vol. 13, pp. S11 – S16, 2003.

[5] D. Schwartz, D. Kim, P. Stupar, J. DeNatale, and R. M’Closkey, “Modal parameter tuning of an axisymmetric resonator via mass perturbation,” *J. Microelectromech. Syst.*, vol. 24, no. 3, pp. 545–555, June 2015.

[6] A. H. Behbahani, D. Kim, P. Stupar, J. DeNatale, and R. T. M’Closkey, “Tailored etch profiles for wafer-level frequency tuning of axisymmetric resonators,” *J. Microelectromech. Syst.*, pp. 1–11, 2017, to appear.

[7] J. L. Atkinson, “Electrostatic bearing,” U.S. Patent 3 334 949, 1967.

[8] J. L. Atkinson and J. C. Boltinghouse, “Speed control for an electrostatically suspended ball gyroscope,” U.S. Patent 3 906 804, 1975.

[9] J. K. Hale, *Oscillations in nonlinear systems*. New York: McGraw-Hill Book Company, Inc., 1963.

[10] J. C. Doyle, B. A. Francis, and A. R. Tannenbaum, *Feedback Control Theory*. New York: Prentice Hall, 1991.